

Supporting Information:  
**Scaling analysis reveals molecular  
mechanism of prion self-replication *in vivo*.**

Georg Meisl, Timothy Kurt, Itzel Condado-Morales,  
Cyrus Bett, Silvia Sorce, Mario Nuvolone, Thomas C T Michaels,  
Daniel Heinzer, Merve Avar, Samuel I A Cohen, Simone Horneman,  
Adriano Aguzzi, Christopher M Dobson, Christina J Sigurdson  
and Tuomas P J Knowles

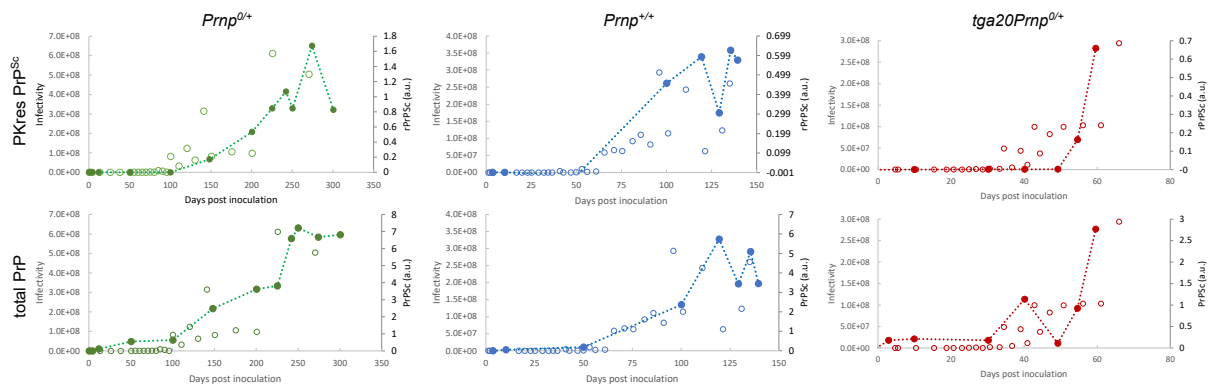


Figure S1: **Extended data 1: Comparison of infectivity and PrP<sup>Sc</sup> from Sandberg *et al.*[14].** The data (open and filled circles) were obtained from Sandberg *et al.*[14] Fig. 1 (PrP measurements, filled circles) and Fig. 2 (infectivity measurement, open circles). The infectivity data are given on a logarithmic scale but are here plotted on a linear scale, with the corresponding values given on the left axis. The PrP<sup>Sc</sup> measurements are plotted on the right axis. Dotted lines connect the PrP<sup>Sc</sup> measurements and are a guide to the eye. There is no clear systematic difference between PrP<sup>Sc</sup> and infectivity when rescaled and both plotted in linear space.

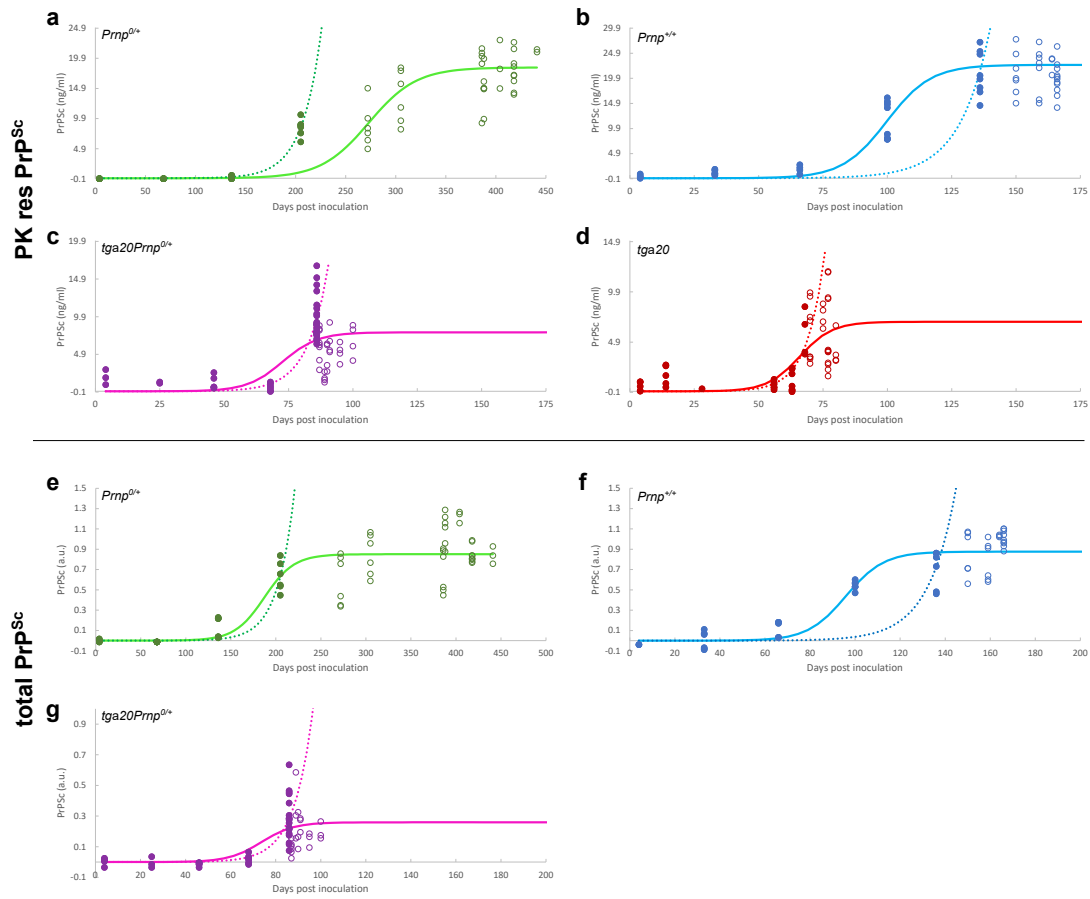


Figure S2: **Extended data 2: Sigmoidal and exponential fits of our data.** Data as shown in the main text (a-d), as well as the data obtained without PK digestion (e-g), fitted to both a sigmoidal function (solid line) and a simple exponential (dotted line). All data points (filled and open circles) are used in the sigmoidal fits, only pre-plateau data points (filled circles) are used in the exponential fits. The data include samples from different mice as well as technical repeats of the ELISA measurements (3-4 at each timepoint).

<i>Prnp</i> <sup>0/+</sup>	<i>Prnp</i> <sup>+/+</sup>	<i>tga20Prnp</i> <sup>0/+</sup>	<i>tga20Prnp</i> <sup>+/+</sup>
4(2)(2)	4(1)(1)	4(2)(2)	4(2)(2)
68(2)(1)	33(2)(2)	25(1)(1)	14(2)(1)
136(2)	66(2)	46(2)	28(2)
205(2)	100(2)	68(2)	42(2)
272(2)	136(2)	86(6)(1)	56(2)
305(2)	150(2)	87(2)	63(2)
386(2)	159(2)	89(1)	68(1)
388(2)	164(1)	90(1)	70(2)
404(1)	166(3)(3)	91(1)(1)	75(1)
418(3)(2)		95(1)	77(3)(2)
441(1)(1)		100(1)(1)	80(1)(1)

Figure S3: **Extended data 3: Summary of numbers of mice used.** Figure 2a of the main text shows the averages of the PrP<sup>C</sup> measurements at early time and terminal disease. Figure 2b-e of shows all technical repeats of the PrP<sup>Sc</sup> ELISA measurements. 3 technical repeats for each mouse are performed for the *Prnp*<sup>0/+</sup> line, 4 technical repeats for all the others. The table gives the time point and the number of mice used in PrP<sup>Sc</sup> ELISA measurements at that timepoint in brackets for each of the lines. The numbers of mice used to determine the early time and terminal disease levels of PrP<sup>C</sup> are also given in green and red, respectively.

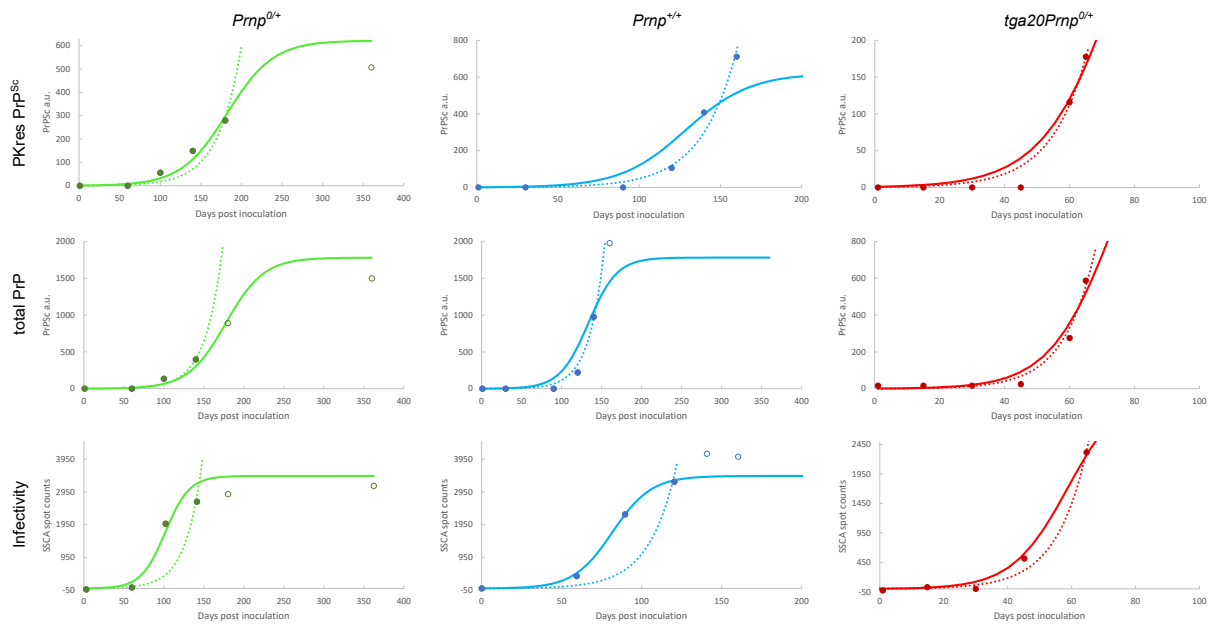


Figure S4: **Extended data 4: Sigmoidal and exponential fits of data from Mays *et al.*[8].** The data (open and filled circles) were obtained from Mays *et al.*[8] Fig. 2 (PrP measurements) and Fig. 4 (infectivity measurement). The data are given for 10 different size fractions, the data here are a sum of all fractions. Fits to both a sigmoidal function (solid line) and a simple exponential (dotted line) are shown. All data points (filled and open circles) are used in the sigmoidal fits, only pre-plateau data points (filled circles) are used in the exponential fits.

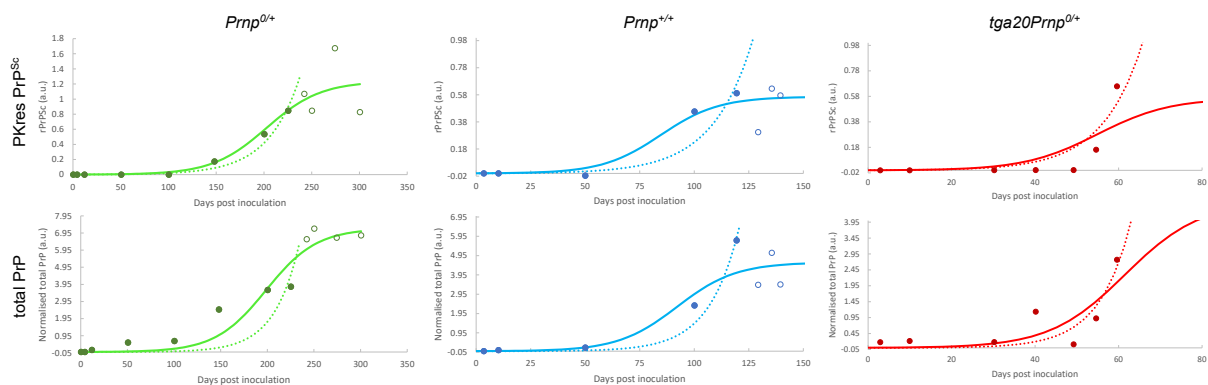


Figure S5: **Extended data 5: Sigmoidal and exponential fits of data from Sandberg *et al.*[14].** The data (open and filled circles) were obtained from Sandberg *et al.*[14] Fig. 1. The infectivity data are given in a logarithmic scale and are analysed separately as detailed at the beginning of this section. Filled circles were used in the fits, open circles were not. The solid line is a fit of the equation  $f(t) = a * \exp(\kappa * t)$  where  $a$  was fixed to a value of  $10^{-3}$  for the PrP data and fitted globally for the infectivity data.

method	measured quantity	scaling	error from regression	mean scaling	mean error
sigmoid high PO	total PrPSc	0.45	0.13	0.46	0.10
sigmoid low PO	total PrPSc	0.49	0.10		
exponential	total PrPSc	0.48	0.08		
lag-time	total PrPSc	0.43	0.07		
sigmoid high PO	Pkres PrPSc	0.56	0.13	0.54	0.11
sigmoid low PO	Pkres PrPSc	0.58	0.10		
exponential	Pkres PrPSc	0.54	0.11		
lag-time	Pkres PrPSc	0.49	0.07		
sigmoid high PO	infectivity	0.41	0.23	0.42	0.24
sigmoid low PO	infectivity	0.39	0.19		
exponential	infectivity	0.46	0.27		

Figure S6: **Extended data 6: Summary of scaling exponents.** The scaling exponents determined from all 3 datasets by the different methods, as well as their standard errors from a linear regression analysis are given. Both the mean value for the scaling and the mean errors are calculated. See Supplementary Note 2 for details.

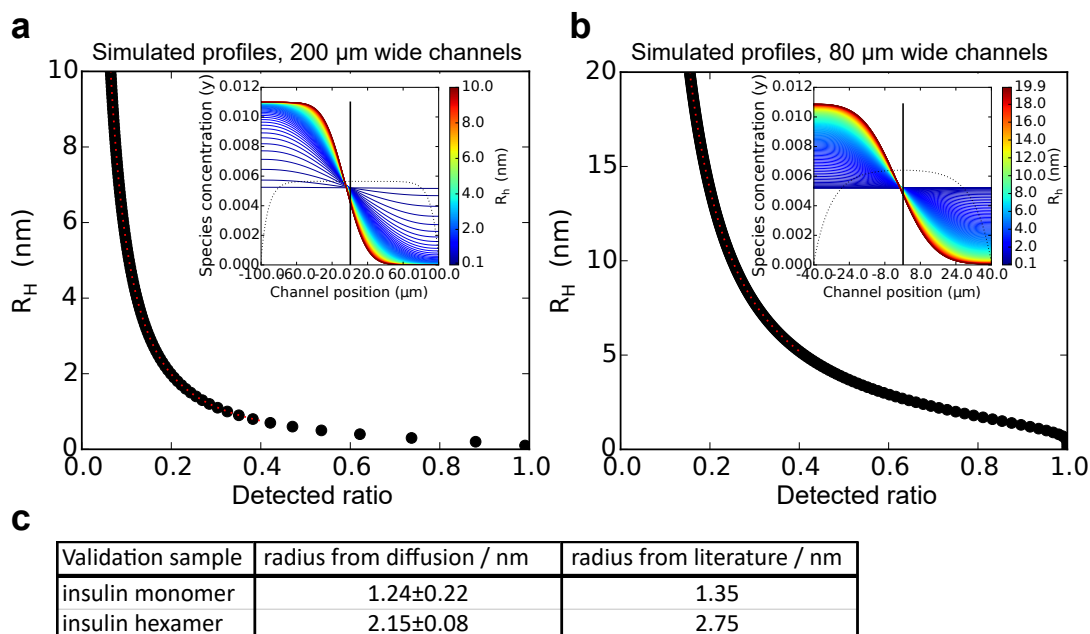


Figure S7: **a,b** Linking the ratio of concentrations in the diffused and diffused halves of the channel to the hydrodynamic radius was accomplished by solving the diffusion equation for the relevant device geometry using finite element integration software. Shown are the results of simulations of the diffusion profiles (inset) and ratio of intensities from the non-diffused channel and the diffused channel,  $f_{nd}/f_d$ , for species with a range of hydrodynamic radii, for the device with 200  $\mu\text{m}$  and 80  $\mu\text{m}$  channel width, respectively. **c** Validation was performed using lyophilised human insulin (Sigma-Aldrich UK). An insulin stock of 10 mg/ml was prepared in 50 mM HCl, filtered through a 22  $\mu\text{m}$  filter. The concentration was measured in the NanoDrop 2000c (ThermoFisher Scientific) by UV-absorbance at 276 nm, using an extinction coefficient value of 1 for 1 mg/ml[1]. Insulin hexamer was prepared as described previously[2]. Monomeric or hexameric samples were injected into the microfluidic device at a total flow rate of 400  $\mu\text{l}/\text{h}$ , using a flow ratio of 19:21 protein to auxiliary buffer. For detection, the commercial HTRF immunoassay kit was used (Cisbio Bioassays, Codolet, France). Samples after diffusion (2  $\mu\text{l}$  per well) were mixed with the antibody-pair (18  $\mu\text{l}$  per well) and incubated for 30 min at room temperature. The TR-FRET readings were performed in Clariostar (BMG Labtech) in the time-resolved fluorescence mode, simultaneously with a standard curve made of 1:2 serial dilutions starting from 2 nM insulin. Quoted values are hydrodynamic radii, errors are standard deviations from 3 repeats, literature values from Oliva *et al.*[11].

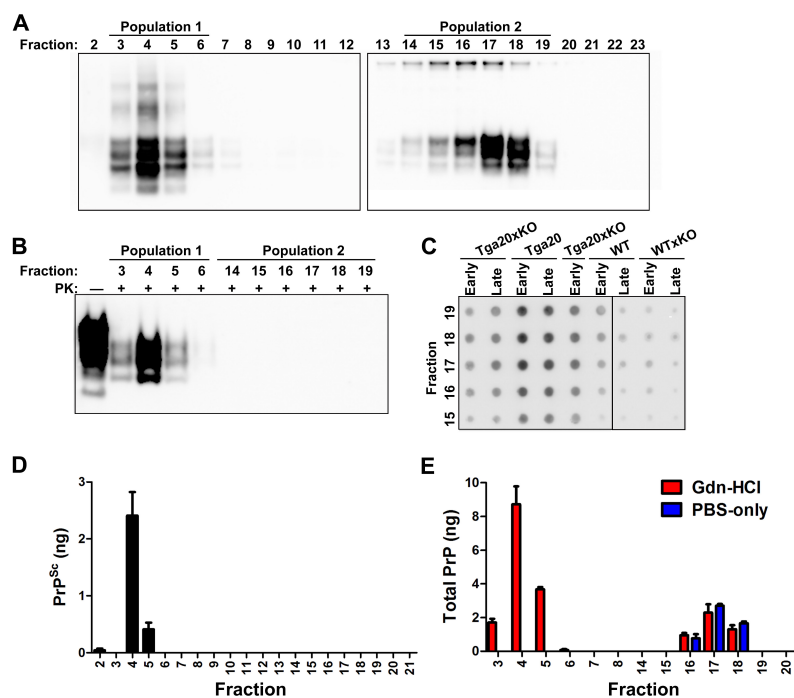


Figure S8: **Extended data: Separation and quantification of PrP<sup>C</sup> and PrP<sup>Sc</sup> from prion-infected animals by centrifugation and size exclusion chromatography.** (A) Brain homogenate from a WT mouse at the terminal stage of disease was subjected to centrifugation followed by FPLC. Aliquots (10  $\mu$ l each) from fractions 2-12 and 13-23 were analysed by SDS-PAGE and western blotting without PK digestion was used to monitor PrP elution from the column, and revealed two distinct populations (indicated at top of panel A). (B) PK digestion (20  $\mu$ g/mL) of aliquots from fractions 3-6 (PrP<sup>Sc</sup>) and 14-19 (PrP<sup>C</sup>) in (A) was used to reveal proteinase-resistant PrP<sup>Sc</sup>. (C) Aliquots (10  $\mu$ l total) from fractions 15-19 of mice (genotype indicated) from shortly after inoculation and at the terminal stage of disease, labelled "early" and "late" respectively, were assessed by semi-quantitative dot blotting. PrP<sup>C</sup> was found primarily in fractions 16-19. (D) Levels of PrP<sup>Sc</sup> in aliquots (10  $\mu$ l total) from (A) as assessed by peptide ELISA. Values were interpolated from a standard curve ( $R^2 = 0.96$ ) generated using recombinant mouse PrP. (E) Aliquots (10  $\mu$ l total) from (A) were mixed with an equal volume of 8 M Gdn-HCl or PBS and heated for 5 min at 80°C prior to ELISA. Gdn-HCl denaturation increases the signal intensity of PrP<sup>Sc</sup> by its disaggregation but does not alter the PrP<sup>C</sup> signals[13, 15]. Samples were run in triplicate and the values were interpolated from a standard curve ( $r^2 = 0.98$ ) generated using recombinant mouse PrP.

# 1 Supplementary Note: Theoretical background and model

We present here a brief derivation of to illustrate the generality of the functional forms we use to fit the experimental data. A more detailed description and discussion of the assumptions can be found in Meisl *et al.* [9]. Let  $G(t)$  denote the concentration of growth competent sites, e.g. the concentration of growth-competent ends in linear aggregation and let  $M(t)$  denote the total aggregated mass. Assuming that the overall increase in mass is dominated by the growth of existing aggregates, the increase in mass is given by

$$\frac{dM}{dt} = k_g G(t) \quad (\text{S1})$$

where  $k_g$  is the rate of growth. Any dependence of growth on the monomer concentration is included in this rate.

If multiplication is the main source of new growth competent sites, and the proceeds independently for each aggregate, as is the case for all common mechanisms of multiplication, such as fragmentation or secondary nucleation, we have

$$\frac{dG}{dt} = k_m M(t) \quad (\text{S2})$$

where  $k_m$  is the rate of multiplication. Both  $k_m$  and  $k_g$  may depend on the monomer concentration. Under the assumption that the monomer concentration is constant, equations S1 and S2 can be solved to yield

$$M(t) = M_0 \cosh(\sqrt{k_g k_m t}) + G_0 \sqrt{\frac{k_g}{k_m}} \sinh(\sqrt{k_g k_m t}) \quad (\text{S3})$$

and

$$G(t) = G_0 \cosh(\sqrt{k_g k_m t}) + M_0 \sqrt{\frac{k_m}{k_g}} \sinh(\sqrt{k_g k_m t}) \quad (\text{S4})$$

where  $M_0$  and  $G_0$  are the values of  $M$  and  $G$  at time 0. In the long time limit the hyperbolic sine and cosine converge simply to the exponential, yielding

$$M(t) \rightarrow \left( M_0 + G_0 \sqrt{\frac{k_g}{k_m}} \right) e^{\sqrt{k_g k_m t}} \quad (\text{S5})$$

Thus, the exponential increase of aggregate mass can be recovered as a very general feature for growth-multiplication type aggregation mechanisms at constant monomer concentrations. We note that the overall exponential rate is the geometric mean of the growth and multiplication rates,  $k_g$  and  $k_m$ , and thus the scaling of this overall rate with

monomer concentration,  $\gamma$ , is given as the arithmetic mean of the scaling of growth and the scaling of multiplication

$$\gamma = \frac{\gamma_m + \gamma_g}{2} \quad (\text{S6})$$

where  $\gamma_g$  and  $\gamma_m$  are the scaling of growth and of multiplication, respectively. Given that growth usually occurs by addition of monomer, its scaling is normally  $\gamma_g = 1$ . The scaling for multiplication can take a wider range of values, such as  $\gamma_m = 0$  for fragmentation.

Finally, consider the average size of an aggregate, which is proportional to the ratio of  $M$  to  $G$ . In the late time limit this is given by

$$\frac{M(t)}{G(t)} \rightarrow \sqrt{\frac{k_g}{k_m}} \quad (\text{S7})$$

which is simply the square root of ratio of the growth rate and the multiplication rate. Therefore, a measurement of the exponential rate,  $\sqrt{k_g k_m}$  together with the average size, can be used to determine both the rates of growth and of multiplication.

## Assumptions and limitations of in vivo model

**Lock-dock growth and intermediate species** Elongation has been shown to proceed by a lock-dock mechanism[5] *in vitro*. The dock step constituting the initial attachment of the monomer to the growing fibril, the lock step the rearrangement of the monomer to adapt the structure of the aggregate and allow for attachment of the next monomer. The lock step dominates the kinetics at high monomer concentration, when the attachment step is fast. The *in vivo* concentrations are however orders of magnitude below the concentrations at which the lock step has been observed to become important, thus we do not consider it explicitly here.

Small oligomeric species have been identified as key species for a number of aggregating proteins. Our models coarse-grain all species larger than monomers into the group of aggregated proteins. The rates obtained are therefore averages over all species considered within the coarse-grained class of aggregate.

Some models consider two different monomeric states, an aggregation-prone state and an inert state. These models are also contained within our general model used here, under the assumption that the two monomeric inter-convert quickly on the timescale of aggregation.

**Clearance** When the removal of aggregates is taken into account, the exponential rate is approximately of the form  $\kappa = \beta m_0^\gamma - k_d$ , where  $\beta$  is the monomer concentration-independent rate constant and  $k_d$  is the clearance rate. Runaway aggregation only occurs for monomer concentrations at which this expression is positive, i.e. when the aggregate amount increases exponentially. As we experimentally observe an exponential increase in all mouse lines, we are in a regime where  $\beta m_0^\gamma > k_d$  at all monomer concentrations.

To illustrate when the presence of clearance has a significant effect on the sampled rates, a rescaled double logarithmic plot of monomer concentration,  $m_0$ , versus rate,  $\kappa$ , for a scaling of  $\gamma = 0.5$  is shown in Fig. S9. This resembles the scaling plots of Fig. 3. Note that for monomer concentrations low enough for clearance to be relevant, a distinctive curvature is visible, for high monomer concentrations the slope of the plots approach the value of  $\gamma$ . As there is no evidence of such curvature in our experimental data, the clearance is likely slow and thus the experimentally observed scaling is a good approximation to  $\gamma$  calculated in the models.

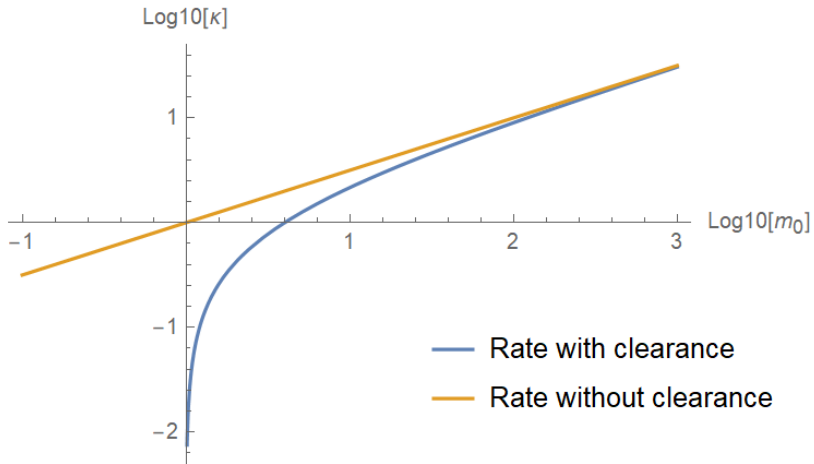


Figure S9: **Scaling of rate with monomer concentration in the presence of clearance** These data are simulated for a molecular scaling exponent  $\gamma = 0.5$ , in the presence of clearance (blue) and in the absence of clearance (orange). Note that in the presence of clearance, for monomer concentrations about an order of magnitude above the minimal monomer concentration required to overcome clearance,  $m_0 = 1$ , the behaviour closely resembles that of the case without clearance.

**Spatial inhomogeneities in aggregation** When the spatial distribution of aggregates over length scales comparable to the size of the brain is taken into account, two limiting regimes can be identified, a replication limit and a spatial spreading limit. In the former scenario, the overall kinetics are dominated by the replication of prions, which is also the case for kinetics observed *in vitro*, for prions as well as other amyloid-related systems[16, 7]. In the latter regime, the overall kinetics are also significantly influenced by spreading of prions through space. We highlight that in all cases the replication of prions is a crucial step in disease progression and is described by the mechanisms discussed in this work. However, in the spatial spreading limit, the overall behaviour does not directly reflect the kinetics of molecular replication but instead also contains contributions from the diffusion or transfer of aggregates to new regions of the brain. There is no evidence for such heterogeneities between brain regions in the PrP<sup>Sc</sup> distribution (as

would be expected if spatial spreading was the limiting factor) under the experimental conditions used in this study (30  $\mu$ l intra-cerebral injection). This may be due to the fact that the initial aggregates are distributed throughout the brain by injection of a relatively large volume, thus decreasing the necessity for spatial spreading and removing this limiting factor. Therefore, we focus here on the replication limit.

**Co-factors** We assume that the involvement of any compounds or co-factors other than PrP<sup>C</sup> can be incorporated into the rate constants, thus giving effective rate constants. As the PrP<sup>C</sup> concentration should be the only relevant quantity that is varied between mouse lines, and other species are thus expected to be present at constant concentrations, this is likely to be a valid assumption, in particular during the initial exponential increase when these co-factors are likely to be present in excess.

**Membranes** As PrP is a membrane-bound protein our models make no specific assumptions about where the reaction takes place and apply as long the measured monomer concentrations are proportional to the concentration of the reacting species, be that a membrane-bound species or one in solution.

## 2 Supplementary Note: Verification of robustness of analysis

In order to highlight the robustness of the conclusion that prion replication in mice has a scaling exponent of approximately 0.5, we used 3 different approaches to extract the rate of replication, all of which gave consistent results. The details are given below. Additionally, we also investigated the effect of varying the assumed initial concentration of prions from inoculation and find our results to be robust to this change as well.

### Sigmoidal and exponential fits

The sigmoidal fitting function, which is the most sophisticated model and is used in the analysis in the main text, is given by  $P_{\max} \left( \left( \frac{P_{\max}}{P_0} - 1 \right) \exp(-\kappa t) + 1 \right)^{-1}$ . It is fitted to all datapoints. For the exponential fits, the data were cut at the last point before the plateau region and then fitted by a simple exponential function  $f(t) = P_0 \exp(\kappa t)$ . The fits are shown in Figs. S4, S5 and S2, the data points used as filled circles. In both functions  $P_0$  was set, as discussed below in section 2.  $P_{\max}$  was allowed to vary for each mouse line if sufficient data points were available to constrain the plateau (data obtained in this work). If insufficient data were available,  $P_{\max}$  was set as a global parameter, i.e. the same for several mouse lines (the same for all mouse lines in Mays *et al.*[8] and the same for the *Prn* $P^{+/+}$  and *tga20* lines for Sandberg *et al.*[14]). The scaling exponent obtained from the exponential fits is shown in Fig. S11, the scaling obtained from the sigmoidal fits in the main text. Both agree well.

### Model-free lag-time analysis

To provide an alternative, model free means to extract the concentration dependence of the replication rate, we here simply consider the time taken to reach a certain threshold concentration of PrP<sup>Sc</sup>. We then use the average time between the last point below the threshold and the first point above the threshold to estimate the time of crossing the threshold. The data are relatively coarse-grained due to the long times between consecutive measurements (often several weeks). The rate is inversely proportional to this time. While to compare this to the absolute rates from the exponential and sigmoidal fits, we would need to determine the constant of proportionality, the scaling exponent is independent of this constant. Therefore, plotting inverse time against PrP<sup>C</sup> concentration on a double logarithmic plot again yields the scaling exponent, see Fig. S10. The scaling exponents obtained in this way are again comparable to those obtained from the sigmoidal fits shown in the main text, which highlights the robustness of the conclusions irrespective of the specifics of the analysis.

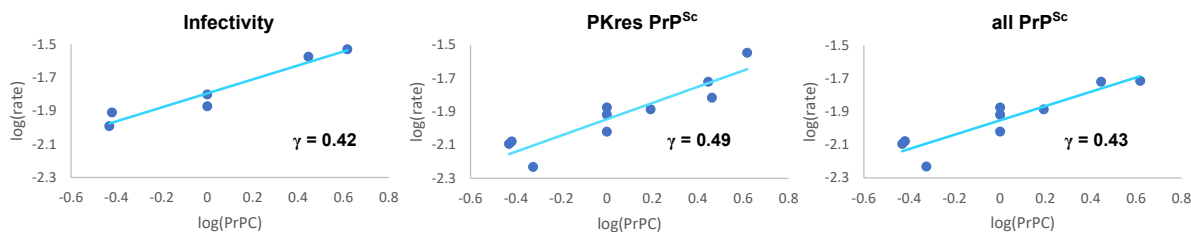


Figure S10: **Relative rates and scaling obtained from lag times.** The thresholds used were 4 ng/ml and 0.25 a.u. for PK resistant and total PrP<sup>Sc</sup> respectively in our data; 0.1 a.u., 1 a.u.  $\cdot 3 \cdot 10^7$  for PK resistant, total PrP<sup>Sc</sup> and infectivity respectively in Sandberg *et al.*[14]; 500 a.u., 100 a.u. and 200 a.u. for infectivity, PK resistant and total PrP<sup>Sc</sup> respectively in Mays *et al.*[8].

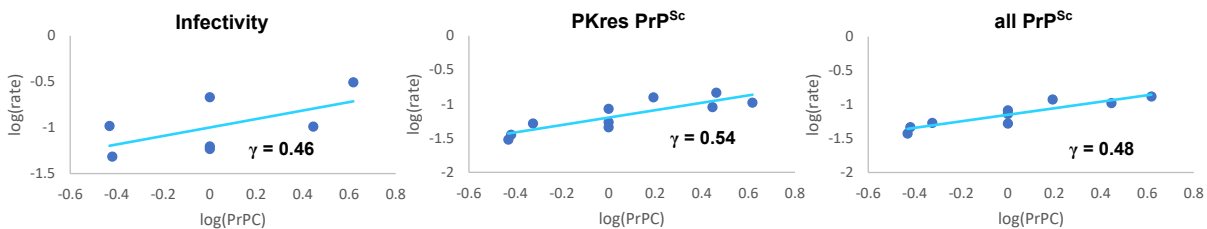


Figure S11: **Exponential rates and scaling obtained from fits of simple exponential to pre-plateau region.** The data and fits are shown in Extended Data Figs. S2, S4 and S5

### Determination and effect of exponential pre-factor

In both the simple exponential  $f(t) = P_0 \exp(\kappa t)$ , as well as the sigmoidal  $P_{\max} \left( \left( \frac{P_{\max}}{P_0} - 1 \right) \exp(-\kappa t) + 1 \right)^{-1}$ , the pre-factor  $P_0$  corresponds to the initial value of the measured quantity, i.e. at time of inoculation. To constrain the fits well,  $P_0$  needs to be fixed, however the exact value of this quantity has only a small effect on the exponential rates and an even smaller effect on their relative differences, as shown in Fig. S12. An upper bound on  $P_0$  can be obtained by considering the initial inoculate: Assuming that the brain used to generate the inoculate had comparable levels of PrP<sup>Sc</sup> and infectivity as the inoculated mouse will display at terminal disease, we can estimate  $P_0$  based on the signal measured at terminal disease and the amount of brain used in inoculation.  $30 \mu\text{l}$  of inoculate were used in all experiments, corresponding to approximately 1/10 of the brain volume. When inoculate was 1% brain homogenate (works by Mays and Sandberg) we thus expect the initial signal to be approximately  $10^{-3}$  of the final signal. In the data obtained in this work, the inoculate was at 0.01%, thus the initial signal is expected to be approximately  $10^{-5}$  of the final signal. To investigate the effect of changing the pre-factor, we decreased its value by two orders of magnitude in each case and refitted

the data using the sigmoidal function. Fits were of equally good quality, the resulting rates were comparable, and the resulting scaling exponents even more so (see Fig. S12). Therefore, the precise choice of pre-factor does not affect our conclusions.

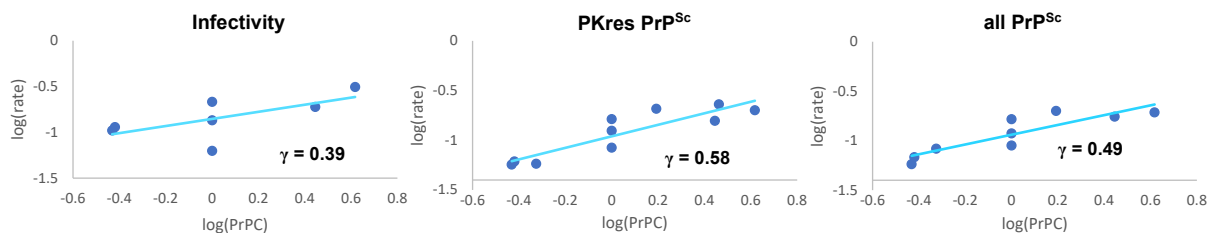


Figure S12: **Exponential rates and scaling obtained with a decreased pre-factor.** We decreased the pre-factor  $P_0$  by two orders of magnitude from the upper bound estimated based on inoculate concentration (used in Fig. 3 of the main text) and amounts and refitted all data with the sigmoidal function.

### 3 Supplementary Note: Additional analysis details

#### Proteinase K resistant, sensitive and total PrP

In this work as well as in Mays *et al.*[8] the concentration of proteinase K resistant PrP<sup>Sc</sup> (in the following referred to as rPrP<sup>Sc</sup>) as well as the total concentration of PrP<sup>Sc</sup>, meaning the combined concentration of rPrP<sup>Sc</sup> and PrP<sup>Sc</sup> that is digested by proteinase K, were determined. Sandberg *et al.*[14] only determined the concentration of rPrP<sup>Sc</sup> and the total concentration of PrP, meaning PrP<sup>C</sup> + rPrP<sup>Sc</sup> + PrP<sup>Sc</sup> that is digested by proteinase K. However, given our knowledge about the time evolution of the PrP<sup>C</sup> concentration we can use these data to estimate the total concentration of PrP<sup>Sc</sup>. The PrP<sup>C</sup> concentration remains approximately constant over the times important for determining the kinetics, and at inoculation the total concentration of PrP<sup>Sc</sup> is expected to be negligible compared to both the PrP<sup>C</sup> concentration. Thus the initial value of the total PrP measured by Sandberg *et al.*[14] should be a good approximation of the PrP<sup>C</sup> concentration, and by subtracting this value from the data at later timepoints we obtain an estimate of the total concentration of PrP<sup>Sc</sup>. The data from Sandberg *et al.*[14] used in the fits of total PrP<sup>Sc</sup> in are processed in this manner.

#### Determination of PrP<sup>C</sup> concentrations

The calculation of the scaling exponent requires knowledge of the PrP<sup>C</sup> concentration for each of these mouse lines. Although PrP<sup>C</sup> concentrations for wild type PrP<sup>0/+</sup> and tga20 mouse lines are expected to be 0.5 and 8 times that of the wild type, actual measurements of the PrP<sup>C</sup> concentration in this work and in the work by Mays *et al.*[8] show that the actual concentrations differ somewhat from these values. Thus, to obtain a scaling from the data in Mays *et al.*[8] we use the values of PrP<sup>C</sup> measured in that work. The PrP<sup>C</sup> concentrations were measured as a function of time, so in order to estimate the overall concentration of PrP<sup>C</sup> we averaged the values measured before the decrease in PrP<sup>C</sup> concentration at late times set in.

As discussed above, Sandberg *et al.*[14] have measured the total concentration of PrP, which we assume is at early times a good measure of the PrP<sup>C</sup> concentration, thus we use these values to obtain the scaling for their data. The PrP<sup>C</sup> concentration from all works are in agreement with our measured values of the PrP<sup>C</sup> concentration, we are thus confident that any inaccuracies in these values will not have a significant effect on the overall scaling.

#### Analysis of PrP<sup>Sc</sup> and infectivity from other works

The infectivity measurements in Sandberg *et al.*[14] are given in logarithmic space, whereas those in Mays *et al.*[8] are given in linear space. A least squares fitting algorithm implicitly assumes homoscedastic noise and thus should be performed in the

space where errors are most evenly distributed. The data infectivity data in Sandberg *et al.*[14] are the only data for which the noise is clearly homoscedastic in logarithmic space, thus these data were analysed by fitting a straight line in logarithmic space (see Fig. 1b in the main text). All other data were fitted in linear space, either to a simple exponential or to a sigmoidal function.

## 4 Supplementary Note: Determination of size of prions

The value of the apparent hydrodynamic radius obtained in this way assumes the diffusing particle is spherical. In the following we will discuss the correction that can be applied to account for non-spherical particles and how to estimate the size of the prion in terms of numbers of monomers from the resulting hydrodynamic radii. For an aspect ratio  $p$ , given by the ratio of length to diameter of a cylindrical particle, the length is given by

$$L = d \left( \ln(p) + 0.312 + \frac{0.565}{p} - \frac{0.1}{p^2} \right) \quad (\text{S8})$$

where  $d$  is the diameter predicted by assuming the diffusing particle is spherical. This phenomenological expression was adapted from Ortega *et al.*[12] and is most accurate for aspect ratios above 2. The volume of the particle is then given by  $V = L\pi(L/p)^2$  and an upper bound for the number of PrP molecules in a prion of a given volume is determined by  $N = V\rho/m_P$  where  $\rho$  is the density of a protein in the aggregate, here assumed to be 1.3 kg/l, and  $m_P$  is the molecular mass of a PrP molecule in the aggregate, in this case this is taken to be 16.5 kDa which is the mass of PrP27-30, the PrP molecule in a prion after PK digestion. Assuming a spherical particle yields an upper bound of 100000 monomers per prion. As previous structural studies point towards spherical aggregates being highly unlikely, this constitutes a conservative upper bound for the number of PrP<sup>C</sup> molecules per aggregate. Structural studies of PrP<sup>Sc</sup> fibrils show that the length of each monomer in the fibril is approximately 1.77 nm[17]. Thus, using this value, we obtain a lower bound when the aspect ratio predicts the prion consisting of a single strand, at an aspect ratio of 264 and a length of 575 monomers per prion. To account for the fact that prions may not consist purely of protein we thus give a conservative lower bound of 100 monomers per prion. For clearly fibrillar prions, the range of predicted numbers of monomers per prion is approximately between 30000 and 3000, (corresponding to aspect ratios of 12 and 85).

## 5 Supplementary Note: Calculation and comparison of rates of growth and multiplication

The concentration of PrP<sup>C</sup> was determined to be 3.1 mg/l in tga20 mice by Mays et. al [8]; the calibration curve in this work used PrP(23-231), which has a molecular mass of approximately 23 kDa [6], thus the molar PrP<sup>C</sup> concentration is 135 nM. To calculate the rate of replication from the rate constants for the *in vitro* measurements, we therefore assumed a monomer concentration of 135 nM.

For A $\beta$ 42, the data in Meisl et al. [10] were used. In this study of the effect of ionic strength on the aggregation behaviour of A $\beta$ 42 we found that, while at high ionic strength the multiplication of A $\beta$ 42 fibrils is dominated by a fibril catalysed secondary nucleation of monomers, at very low ionic strengths, fragmentation may also play a role. We concluded that this was most likely because secondary nucleation was slowed significantly at low ionic strengths, thus making fragmentation kinetically visible. Fragmentation of fibrils likely also occurs at higher ionic strengths, but was not visible because secondary nucleation is much faster. However, these *in vitro* measurements were performed at  $\mu$ M concentrations, so when extrapolating to 135 nM for this work, the rates of secondary nucleation will be slower by several orders of magnitude. By contrast, fragmentation does not depend on the monomer concentration, so will not be slower at 135 nM. Thus, like a decrease ionic strength, a decrease in monomer concentration could lead to fragmentation being the dominant mechanism of multiplication. To estimate the replication rate at 135 nM we thus assume that A $\beta$ 42 fibrils fragment at the same rate as observed in the low ionic strength experiments, and elongate at the rate observed under physiological ionic strength conditions [4]. If we instead assume that secondary nucleation is still dominant at 135 nM and extrapolate from the rates in Cohen *et al.* [3], the predicted rates of replication and multiplication are one and two orders of magnitude lower respectively.

## References

- [1] Atta Ahmad, Vladimir N. Uversky, Dongpyo Hong, and Anthony L. Fink. Early events in the fibrillation of monomeric insulin. *Journal of Biological Chemistry*, 280(52):42669–42675, 2005.
- [2] Curtis R. Bloom, Wonjae E. Choi, Peter S. Brzovic, Julie J. Ha Sheng-Tung Huang, Niels C. Kaarsholm, and Michael F. Dunn. Ligand binding to wild-type and e-b13q mutant insulins: A three-state allosteric model system showing half-site reactivity. *Journal of Molecular Biology*, 245(4):324 – 330, 1995.
- [3] Fred E Cohen and Jeffery W Kelly. Therapeutic approaches to protein-misfolding diseases. *Nature*, 426(6968):905–909, Dec 2003.
- [4] Samuel I. A. Cohen, Sara Linse, Leila M. Luheshi, Erik Hellstrand, Duncan A. White, Luke Rajah, Daniel E. Otzen, Michele Vendruscolo, Christopher M. Dobson, and Tuomas P. J. Knowles. Proliferation of amyloid-beta42 aggregates occurs through a secondary nucleation mechanism. *Proceedings of the National Academy of Sciences*, 110:9758–9763, 2013.
- [5] William P. Esler, Evelyn R. Stimson, Joan M. Jennings, Harry V. Vinters, Joseph R. Ghilardi, Jonathan P. Lee, Patrick W. Mantyh, and John E. Maggio. Alzheimer’s disease amyloid propagation by a template-dependent dock-lock mechanism. *Biochemistry*, 39(21):6288–6295, May 2000.
- [6] Simone Hornemann, Carsten Korth, Bruno Oesch, Roland Riek, Gerhard Wider, Kurt Wüthrich, and Rudi Glockshuber. Recombinant full-length murine prion protein, mprp(23–231): purification and spectroscopic characterization. *FEBS Letters*, 413(2):277 – 281, 1997.
- [7] Tuomas P J Knowles, Christopher A Waudby, Glyn L Devlin, Samuel I A Cohen, Adriano Aguzzi, Michele Vendruscolo, Eugene M Terentjev, Mark E Welland, and Christopher M Dobson. An analytical solution to the kinetics of breakable filament assembly. *Science*, 326(5959):1533–1537, 2009.
- [8] Charles E. Mays, J van der Merwe, C Kim, T Haldiman, D McKenzie, JG Safar, and D Westaway. Prion infectivity plateaus and conversion to symptomatic disease originate from falling precursor levels and increased levels of oligomeric prpsc species. *J Virol.*, 24(89):12418–12426, 2015.
- [9] Georg Meisl, Alexander J. Dear, Thomas C. T. Michaels, and Tuomas P. J. Knowles. Mechanism, scaling and rates of protein aggregation from in vivo measurements. *arXiv*, 2008.09699, 2020.

- [10] Georg Meisl, Julius B. Kirkegaard, Paolo Arosio, Thomas T. C. Michaels, Michele Vendruscolo, Christopher M. Dobson, Sara Linse, and Tuomas P. J. Knowles. Molecular mechanisms of protein aggregation from global fitting of kinetic models. *Nature Protocols*, 11(2):252–272, 2016.
- [11] Alexis Oliva, José Fari na, and Matias Llabrés. Development of two high-performance liquid chromatographic methods for the analysis and characterization of insulin and its degradation products in pharmaceutical preparations. *Journal of Chromatography B: Biomedical Sciences and Applications*, 749(1):25 – 34, 2000.
- [12] A. Ortega and J. Garcia de la Torre. Hydrodynamic properties of rodlike and disklike particles in dilute solution. *The Journal of Chemical Physics*, 119(18):9914–9919, 2003.
- [13] J. Safar, H. Wille, V. Itri, D. Groth, H. Serban, M. Torchia, F. E. Cohen, and S. B. Prusiner. Eight prion strains have prp(sc) molecules with different conformations. *Nat Med*, 4(10):1157–1165, Oct 1998.
- [14] Malin K. Sandberg, Huda Al-Doujaily, Bernadette Sharps, Michael Wiggins De Oliveira, Christian Schmidt, Angela Richard-Londt, Sarah Lyall, Jacqueline M. Linehan, Sebastian Brandner, Jonathan D. F. Wadsworth, Anthony R. Clarke, and John Collinge. Prion neuropathology follows the accumulation of alternate prion protein isoforms after infective titre has peaked. *Nat Commun*, 5:4347, 2014.
- [15] Dan Serban, Albert Taraboulos, Stephen J. DeArmond, and Stanley B. Prusiner. Rapid detection of creutzfeldt-jakob disease and scrapie prion proteins. *Neurology*, 40(1):110, 1990.
- [16] Jan Stöhr, Nicole Weinmann, Holger Wille, Tina Kaimann, Luitgard Nagel-Steger, Eva Birkmann, Giannantonio Panza, Stanley B Prusiner, Manfred Eigen, and Detlev Riesner. Mechanisms of prion protein assembly into amyloid. *Proc Natl Acad Sci U S A*, 105(7):2409–2414, Feb 2008.
- [17] Holger Wille and Jesus R Requena. The structure of prp(sc) prions. *Pathogens*, 7:20, 2018.